Osinga, H. M. (2003). Two-dimensional invariant manifolds in four-dimensional dynamical systems. DOI: 10.1016/j.cag.2004.12.016

Two-dimensional invariant manifolds in four-dimensional dynamical systems

Hinke Osinga*
Department of Engineering Mathematics, University of Bristol
Bristol BS8 1TR, UK
E-mail: H.M.Osinga@bristol.ac.uk

December 22, 2003

Abstract

This paper explores the visualization of two-dimensional stable and unstable manifolds of the origin (a saddle point) in a four-dimensional Hamiltonian system arising from control theory. The manifolds are computed using an algorithm that finds sets of points that lie at the same geodesic distance from the origin. By coloring the manifolds according to this geodesic distance, one can gain insight into the geometry of the manifolds and how they sit in four-dimensional space. This is compared with the more conventional method of coloring the fourth coordinate. We also take advantage of the symmetries present in the system, which allow us to visualize the manifolds from different viewpoints at the same time.

Keywords: Hamiltonian system, dynamical system, global unstable manifolds, optimal control theory.

*Corresponding author: Tel: +44 (0)117 928-7600, Fax: +44 (0)117 954-6833

1 Introduction

The computation of stable and unstable manifolds in vector fields has recently become a field of renewed activity; see [1, 6, 7] and the recent publications [2, 4, 8]. Several new algorithms have been developed and, even though attention remains focussed on low-dimensional systems, higher-dimensional problems are beginning to attract more interest as well. The main goal for computing stable and unstable manifolds is to gain insight into their geometry and how they are embedded in phase space. As a consequence, the visualization of the manifolds is as important as the actual computational challenge. For higher-dimensional dynamical systems, it is already hard to visualize one- or two-dimensional manifolds. In particular, the projection used in the visualization may result in self-intersection of the manifolds. This makes it much harder to assess the structure of the manifolds, for example, whether two manifolds form a heteroclinic tangle or not.

In this paper we explore aspects of visualizing two-dimensional manifolds of a four-dimensional dynamical system. We consider a model arising in optimal control and the manifolds are stable and unstable manifolds of the origin (a saddle equilibrium) of a Hamiltonian system. The figures are rendered with the package Geomview [11], which is also used for the animations in the associated multimedia supplement [14].

It is already a serious challenge to accurately compute two-dimensional manifolds in four dimensions. The algorithm used to compute the manifolds in this paper is described in detail in [8]. This algorithm produces a data file that can be visualized with the package Geomview [11]. Geomview actually displays this data in a four-dimensional space, that is, the automatic shadow effects are created by a light source in four-dimensional space, but it is very hard to interpret the result. The human eye is very good at perceiving depth in a flat-screen picture, but our intuition fails when we try to do this for a projection of an object that sits in a four-dimensional space.

One way to enhance the visualization is the clever use of color. In a particular projection onto three of the four coordinates, the manifold can be visualized using a color that varies with the fourth (missing) coordinate. In particular, (self-)intersections of the manifolds can be identified quickly this way, since an intersection is a true intersection only if the color matches. This paper explores another way of using color in the visualization, namely coloring the manifold according to its geometry. The algorithm in [8] computes a two-dimensional manifold of a saddle (the origin in our example)

as a set of topological circles that consist of all points that lie at the same geodesic distance to the saddle; the geodesic distance between two points is the arclength of the shortest path between these two points that lies entirely on the manifold. By assigning a different color to each of these *geodesic level sets* we obtain a visualization where the color indicates how far the points are from the origin along the manifold. Effectively, this technique also helps to perceive depth in the direction that is missing in the projection.

The Hamiltonian system in our example has special symmetries which implies that the stable and unstable manifolds of the origin also satisfy certain symmetry properties. By taking advantage of these symmetries, together with the above two different methods of coloring the manifolds, we can emphasize different properties of the manifolds and learn how to "look into" four-dimensional space. This paper is accompanied by a multimedia supplement [14] showing animations of the manifolds, which provide another useful tool for visualization in four-dimensional space.

This paper is organized as follows. In the next section we introduce the Hamiltonian dynamical system and explain how it is related to optimal control theory. Section 3 introduces the (global) stable and unstable manifolds of the origin and describes the symmetries present in the dynamical system. The computation and visualization of the stable and unstable manifolds is presented in Sec. 4. We end with conclusions in Sec. 5.

2 Four-dimensional Hamiltonian system

We consider a four-dimensional Hamiltonian system that arises when studying the optimal control problem of balancing an inverted pendulum on a cart subject to a quadratic cost fuction; a detailed introduction of this control problem can be found in [3]. The frictionless pendulum has a two-dimensional phase space and the motion is controlled by applying a horizontal force to the cart in the plane of motion of the pendulum. If the mass of the cart is M, the (uniformly distributed) mass of the pendulum m and the center of mass of the pendulum is at distance l from the pivot, then the equations of

motion are

$$\left\{\begin{array}{rcl} \dot{x}_1 &=& x_2, \\ \dot{x}_2 &=& f(x) + c(x)\,u \\ &:=& \dfrac{\frac{g}{l}\sin(x_1) - \frac{1}{2}\frac{m}{m+M}\,x_2^2\sin(2x_1)}{\frac{4}{3} - \frac{m}{m+M}\,\cos^2(x_1)} - \dfrac{\frac{1}{l\,(m+M)}\,cos(x_1)}{\frac{4}{3} - \frac{m}{m+M}\,\cos^2(x_1)}\,u, \end{array}\right. \tag{1}$$

where g is the gravitational constant. Here $x = (x_1, x_2)^T \in \mathbb{R}^2$ is the phase space with x_1 the offset angle from the upright position and x_2 the angular velocity. Hence, the origin corresponds to the stationary upright position. For simplicity, we ignore the motion of the cart.

The aim is, for given initial condition x_0, to find a control function $u = u(t)$ such that the solution $x(t)$ of (1), with $x(0) = x_0$ and using $u(t)$, converges to the origin. There will typically be many control functions achieving this aim. However, we seek to minimize the cost given as the function

$$V(x_0) = \min_{u:[0,\infty)\to\mathbb{R}} \quad \int_0^\infty Q(x(t), u(t))\,dt,$$

where

$$Q(x, u) = \mu_1 x_1^2 + \mu_2 x_2^2 + \mu_3 u^2 \tag{2}$$

for positive parameters μ_1, μ_2 and μ_3. Note that $Q(x, u)$ is not periodic in the angle x_1, which means that we penalize the upright position if it is an integer number of full rotations away from the origin.

One can think of this problem as a paradigm for nonlinear optimal control problems [3, 5, 9]. In general, under suitable assumptions, an optimal control problem can be formulated as a Hamiltonian system defined on a phase space of twice the dimension. The optimal solutions are then found as trajectories that converge to the origin of the Hamiltonian system, which corresponds to the origin, the target, in the control problem; see [12, 13] for more details.

In this particular example we can construct the Hamiltonian formulation explicitly. We enlarge the phase space by adding the so-called dual variable $p = (p_1, p_2)^T \in \mathbb{R}^2$. The Hamiltonian system is then defined for $(x_1, x_2, p_1, p_2)^T \in \mathbb{R}^4$ and the equations of motion are dictated by the Hamiltonian $H(x, p) = H(x_1, x_2, p_1, p_2)$ which involves the motion defined by Eq. (1) and the cost function Eq. (2). More precisely, $H(x, p) = K(x, p, u^*)$, where $K(x, p, u)$ is the so-called *pre-Hamiltonian*

$$K(x, p, u) = Q(x, u) + p^T \begin{bmatrix} x_2 \\ f(x) + c(x)\,u \end{bmatrix}, \tag{3}$$

and $u = u^*(x,p)$ is the (unique) control that minimizes $K(x,p,u)$. It is straightforward to find

$$u^*(x,p) = -\frac{1}{2\mu_3}\, p_2\, c(x) \tag{4}$$

and, thus, the Hamiltonian becomes

$$H(x,p) = \mu_1 x_1^2 + \mu_2 x_2^2 + \frac{c(x)^2}{4\mu_3} + p_1 x_2 + p_2\, f(x) - \frac{p_2}{2\mu_3}\, c(x)^2. \tag{5}$$

This leads to the dynamical system:

$$\left\{\begin{array}{rcccl} \dot{x}_1 &=& \dfrac{\partial H}{\partial p_1} &=& x_2, \\ \dot{x}_2 &=& \dfrac{\partial H}{\partial p_2} &=& f(x) - \dfrac{p_2}{2\mu_3}\, c(x)^2, \\ \dot{p}_1 &=& -\dfrac{\partial H}{\partial x_1} &=& -2\mu_1 x_1 - p_2 \dfrac{\partial f(x)}{\partial x_1} + \dfrac{p_2^2}{2\mu_3} c(x) \dfrac{\partial c(x)}{\partial x_1}, \\ \dot{p}_2 &=& -\dfrac{\partial H}{\partial x_2} &=& -2\mu_2 x_2 - p_1 - p_2 \dfrac{\partial f(x)}{\partial x_2} + \dfrac{p_2^2}{2\mu_3} c(x) \dfrac{\partial c(x)}{\partial x_2}. \end{array}\right. \tag{6}$$

From the optimal control point of view one is interested in those trajectories of Eq. (6) that converge to the origin in forward time using $u = u^*(x,p)$, for which the total cost is (locally) minimal. Indeed, if one projects a trajectory $(x(t), p(t))$ that satisfies Eq. (6) onto the plane $x(t)$, the resulting orbit is a solution of Eq. (1) with $u = u^*(x,p)$. Namely, the equations for x_1 and x_2 are identical to those of Eq. (1) provided $u = u^*(x,p)$.

We now focus on Eq. (6) and study the global stable and unstable manifolds of the origin in this four-dimensional phase space. To this end, we fix the parameters as in [3], namely, $m = 2\,\mathrm{kg}$, $M = 8\,\mathrm{kg}$, $l = 0.5\,\mathrm{m}$, $g = 9.8\,\mathrm{m/s^2}$, $\mu_1 = 0.1$, $\mu_2 = 0.05$ and $\mu_3 = 0.01$.

3 Two-dimensional invariant manifolds

Equation (6) has a single equilibrium, namely the origin. The eigenvalues of the Jacobian matrix evaluated at the origin are, numerically,

$$-4.349382195, \quad -3.978293499, \quad 3.978293499, \quad \text{and} \quad 4.349382195.$$

This means that the origin is a saddle with two-dimensional stable and two-dimensional unstable eigenspaces. The Stable Manifold Theorem [10] guarantees the existence of two-dimensional stable and unstable manifolds locally near the origin tangent at the origin to the respective eigenspaces. Globally these manifolds are two-dimensional immersed manifolds in $\mathbb{R}^4$, uniquely defined as

$$\begin{aligned} W^s(0) &= \{q \in \mathbb{R}^4 \mid \lim_{t\to\infty} \phi^t(q) = 0\}, \\ W^u(0) &= \{q \in \mathbb{R}^4 \mid \lim_{t\to-\infty} \phi^t(q) = 0\}, \end{aligned}$$

where $\phi^t(\cdot)$ is the solution operator (the flow) for Eq. (6) and the supscripts s and u stand for stable and unstable, respectively. Both manifolds are as smooth as the vector field itself.

Recall that the set of optimal solutions to (1-2) is characterized by trajectories of Eq. (6) that converge to the origin. It follows that this set is given by the stable manifold $W^s(0)$ of the origin of Eq. (6). Note that the given smoothness of $W^s(0)$ implies that the control $u = u^*(x, p)$, which achieves the optimal cost, always exists and is smooth; we refer to [3] for more details. In this paper we address the fact that, from the optimal control point of view, one is interested in the geometry of $W^s(0)$ as a subset of $\mathbb{R}^4$. Namely, if two initial conditions on $W^s(0)$ project to the same point in the (x_1, x_2)-plane, then there exist two different trajectories that are both (locally) optimal. Hence, the visualization of $W^s(0)$ is crucial for gaining insight in the structure of the optimal solution set.

The change of coordinates

$$(t, x_1, x_2, p_1, p_2) \mapsto (-t, x_1, -x_2, -p_1, p_2) \tag{7}$$

leaves the system unchanged. Note the reversal of time that is necessary here. This means that $W^s(0)$ is, in fact, equal to $W^u(0)$ after a reflection in the (x_2, p_1)-plane.

Furthermore, the system is invariant under the transformation

$$(t, x_1, x_2, p_1, p_2) \mapsto (-t, -x_1, x_2, p_1, -p_2). \tag{8}$$

Since time is again reversed, we find that $W^s(0)$ and $W^u(0)$ are each other's mirror images via reflection in the (x_1, p_2)-plane. The composition of the transformations (7) and (8) is

$$(t, x_1, x_2, p_1, p_2) \mapsto (t, -x_1, -x_2, -p_1, -p_2),$$

which means that both $W^s(0)$ and $W^u(0)$ are invariant under point rotation by π about the origin.

4 Visualization of the manifolds

Both $W^s(0)$ and $W^u(0)$ were computed using the algorithm described in [8]. This algorithm grows the manifold starting from a small disc centered at the origin and contained in the two-dimensional linear eigenspace associated with the stable or unstable eigenvalues, respectively. The manifolds are grown by adding rings of points that lie at equal geodesic distance to the origin. Each such ring, or geodesic level set, forms a smooth topological circle, which is obtained pointwise by solving an appropriate boundary value problem for each mesh point on it; see [8] for a more detailed explanation of the algorithm.

We computed $W^s(0)$ and $W^u(0)$ up to (approximately) geodesic distance 26.25. The integration of the vector field was done using fixed stepsize Runge Kutta of order four. The integration stepsize was 0.001. For both manifolds we started with an initial circle of 20 points in the respective eigenspaces at radius 1.0 from the origin. Subsequent rings are represented by a finite number of mesh points that are approximately uniformly distributed with maximal mesh distance 0.5. The distance between successive rings is determined by the curvature of the manifold. In total, we calculated 111 rings on each manifold with 1229 mesh points on the last geodesic level set.

We remark here that both $W^s(0)$ and $W^u(0)$ were calculated with the algorithm and we did not take advantage of the symmetry in the system. In fact, not even the start data was invariant under rotation by π. Furthermore, our approximation of $W^s(0)$ is not identical to our approximation of $W^u(0)$ after reflection in either the (x_1, p_2)- or the (x_2, p_1)-plane. However, the computed manifolds are invariant under these transformations up to the computational accuracy. This constitutes an independent accuracy assessment of the computations.

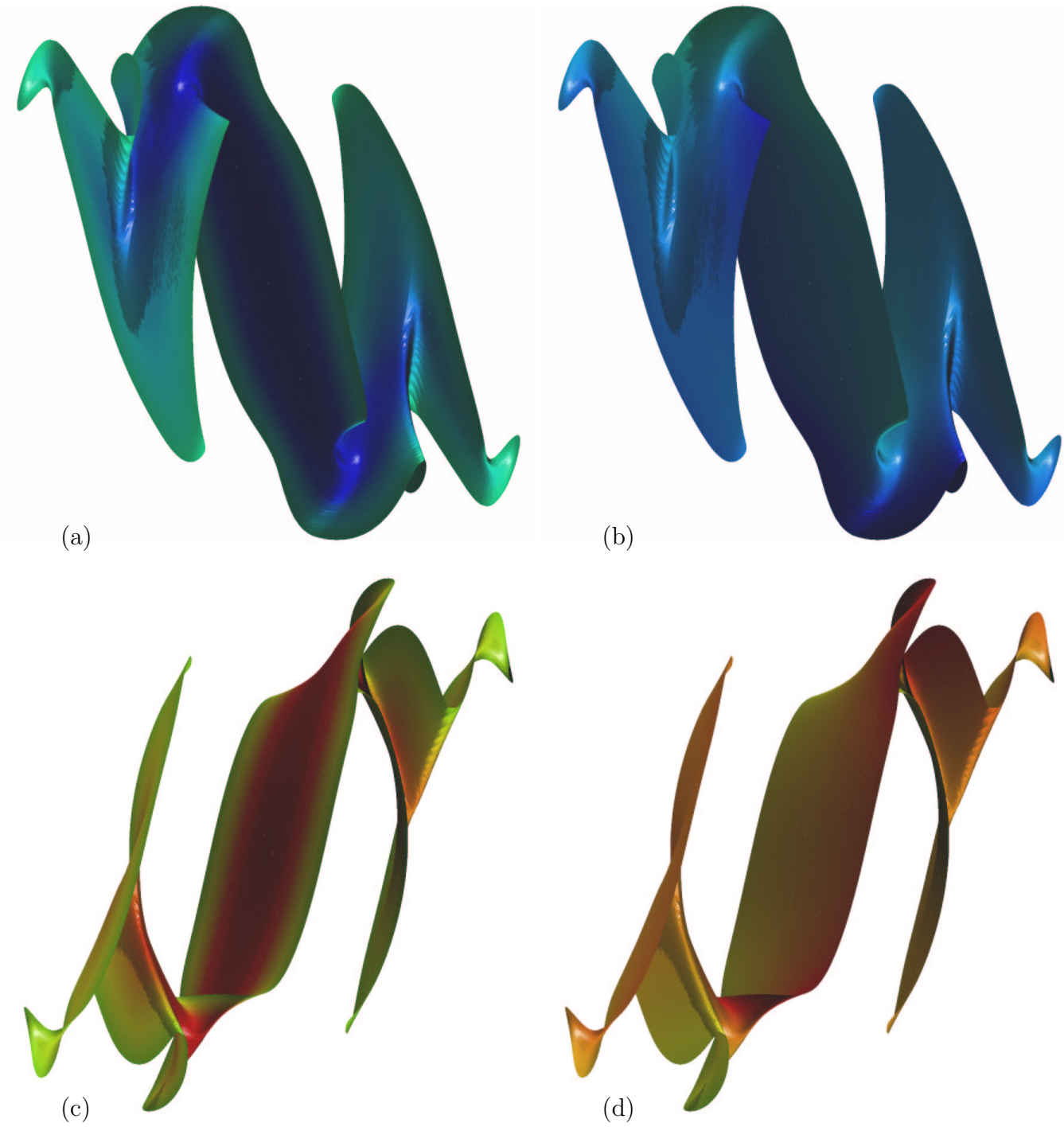

Figure 1: The stable and unstable manifolds of the origin of Eq. (6). In all four panels the manifolds are projected onto the (x_1, x_2, p_1)-hyperplane in $\mathbb{R}^4$ and the axes perpendicular to the page are the vectors $(0, 0, 0, 1)$ and $(-\sin(\frac{\pi}{30}), 0, \cos(\frac{\pi}{30}), 0)$. Panels (a) and (b) show $W^s(0)$ and panels (c) and (d) show $W^u(0)$. The manifolds are colored according to geodesic distance in panels (a) and (c), and according to the value of the p_2-coordinate in panels (b) and (d).

The stable manifold is shown in Figs. 1(a) and (b), while Figs. 1(c) and (d) visualize $W^u(0)$. We used the same projection in all four panels of Fig. 1, namely a projection along the p_2-axis and a rotation by $-\frac{\pi}{30}$ in the (x_1, p_1)-plane. Each manifold is visualized using two different coloring methods. In Figs. 1(a) and (c) $W^s(0)$ and $W^u(0)$ are colored according to geodesic distance to the origin. This means that each geodesic level set is assigned a unique color. For Fig. 1(a) the colors run from dark blue (geodesic distance 0) via cyan to green (geodesic distance 26.25), while in Fig. 1(c) they run from red (geodesic distance 0) via yellow to green (geodesic distance 26.25). The sense of depth in the p_2-coordinate is visualized in panels (b) and (d) of Fig. 1, where the color is determined by the value of the p_2-coordinate. The range of p_2 is from -20.0 to 20.0, which is represented by a color from blue to green in Fig. 1(b), and from red to green in Fig. 1(d).

The symmetry properties of the manifolds have the advantage that we can obtain information about $W^s(0)$ from $W^u(0)$ (and vice versa). The picture of $W^u(0)$ is the same as $W^s(0)$ viewed 'from the other side,' that is, along the vectors $(0, 0, 0, -1)$ and $(-\sin(\frac{\pi}{30}), 0, -\cos(\frac{\pi}{30}), 0)$. This is best seen by observing that the p_2-coordinate in Fig. 1(b) decreases from 'top' to 'bottom' while it increases in Fig. 1(d). Panels (a) and (c) in Fig. 1 give a better sense of the depth of the projection in (x_1, x_2, p_1)-space, because the 'front' and 'back' of the level sets are at equal geodesic distance to the origin.

Figure 2 shows both manifolds together in (x_1, x_2, p_1)-space. As before, panel (a) shows the manifolds colored according to geodesic distance, while the p_2-coordinate is used for the coloring in panel (b). This figure clearly illustrates the problem of visualizing objects in four-dimensional space. Namely, the unstable manifold clearly seems to self-intersect, which is not possible for an invariant manifold of a Hamiltonian system. Hence, this intersection is due to the projection. However, $W^s(0)$ and $W^u(0)$ can intersect, so how can one distinguish such genuine intersections from intersections due to the projection? Figure 2 is accompanied by an animation that rotates the manifolds in (x_1, x_2, p_1)-space [14]. If an intersection is a genuine intersection, then it will not disappear when rotating the manifolds. Compare, for example, Fig. 2(a) with Fig. 4(a), which shows the two manifolds in the same space, but slightly rotated (about the anti-diagonal as seen on the page); the equivalent picture for Fig. 2(b) can be seen in Fig. 5(a).

As mentioned before, the symmetry properties of Eq. (6) are such that $W^u(0)$ can be interpreted as $W^s(0)$ viewed from a different side. There are two planes of symmetry, namely the (x_1, p_2)-plane and the (x_2, p_1)-plane.

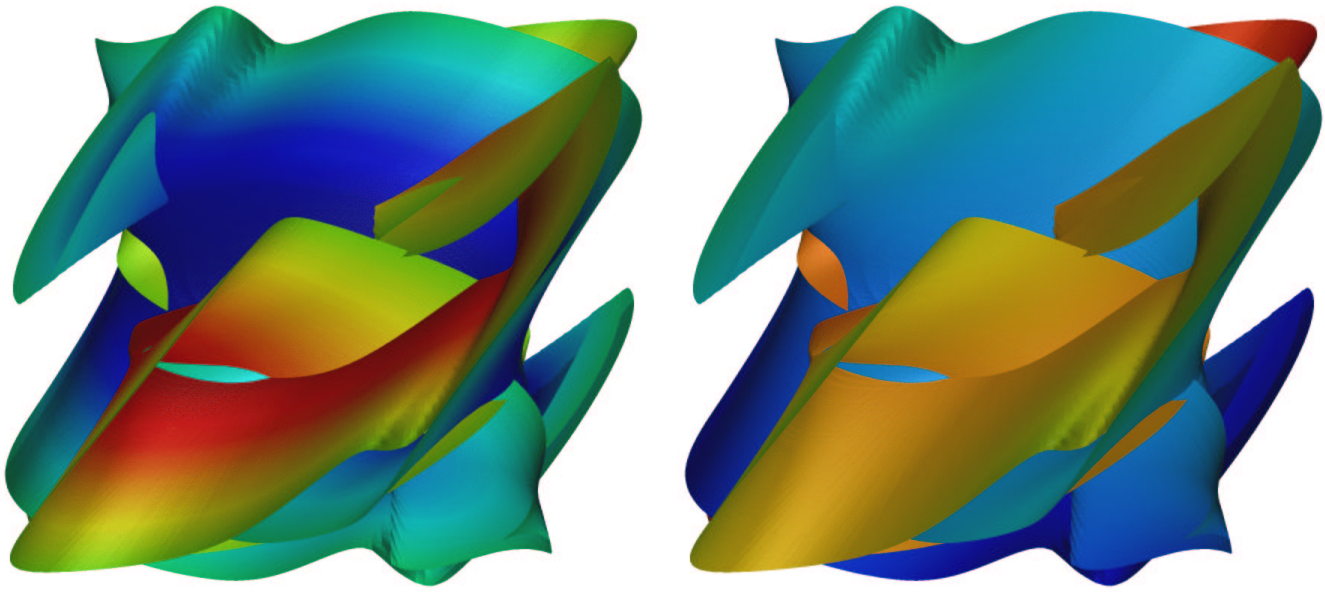

(a) (b)

Figure 2: The stable and unstable manifolds of the origin of Eq. (6) projected into (x_1, x_2, p_1)-space. The manifolds are colored according to geodesic distance to the origin in panel (a), and according to the value of the p_2-coordinate in panel (b). This figure is accompanied by an animation where the manifolds are rotated in (x_1, x_2, p_1)-space [14].

Since in all of our figure we project the manifolds along a coordinate axis, one of these planes always collapses to a line. However, the other plane of symmetry is typically visible, because $W^s(0)$ and $W^u(0)$ must be equal on these planes. That is, $W^s(0)$ and $W^u(0)$ intersect along planar curves that lie in the (x_1, p_2)-plane or the (x_2, p_1)-plane.

Figure 3 shows $W^s(0)$ and $W^u(0)$ in a projection where the effect of the symmetry is clearly present. Here we view the manifolds in (x_2, p_1, p_2)-space. The coloring in panel (a) is according to geodesic distance, as before. In panel (b) the value of the x_1-coordinate, ranging between ± 10.533, was used to color the manifolds. The stable manifold is colored using the range from blue to green, while the unstable manifold uses red to green coloring. The two manifolds clearly intersect along what appears to be a straight line. There are other intersections as well. Most are self-intersections due to the

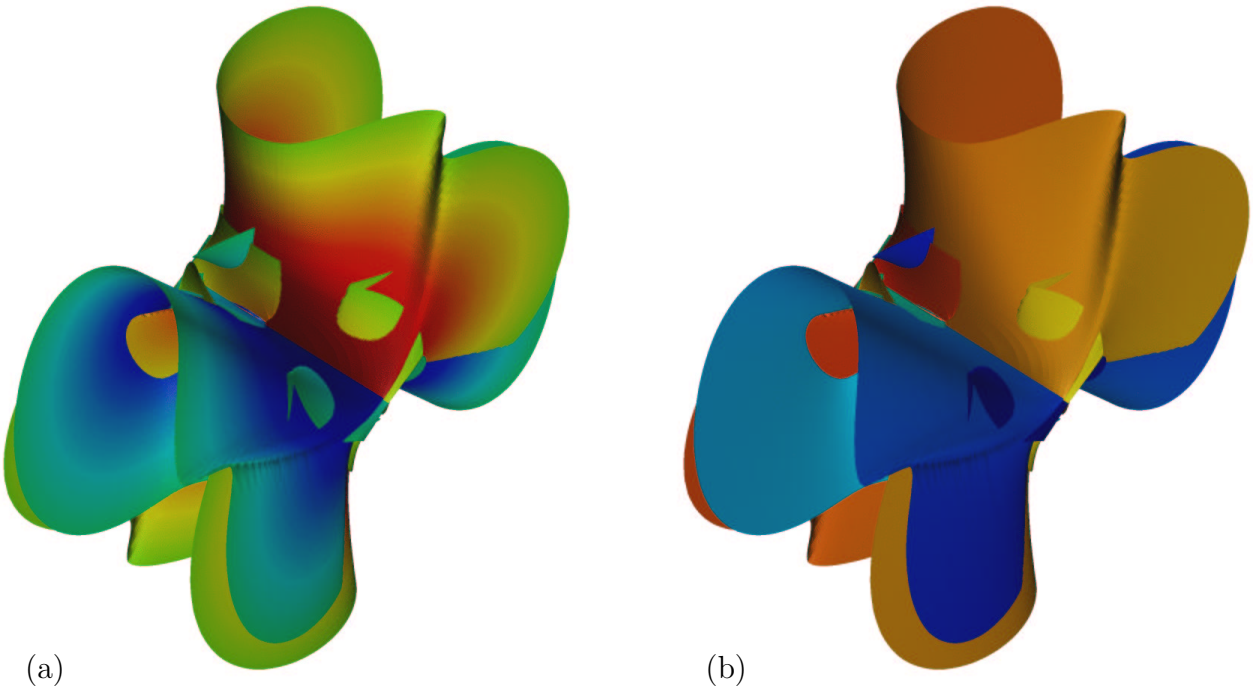

(a) (b)

Figure 3: The stable and unstable manifolds of the origin of Eq. (6) projected into (x_2, p_1, p_2)-space. The manifolds are colored according to geodesic distance to the origin in panel (a), and according to the value of the x_1-coordinate in panel (b). This figure is accompanied by an animation where the manifolds are rotated in (x_2, p_1, p_2)-space [14].

projection, but these do not lie in the (x_2, p_1)-plane of symmetry.

We can use the obvious location of the plane of symmetry to examine possible intersections of $W^s(0)$ and $W^u(0)$. For example, consider how $W^u(0)$ is situated above $W^s(0)$ in the top part of Fig. 3(b). On the right side towards the boundary of the computed manifolds, $W^s(0)$ and $W^u(0)$ appear to intersect. However, symmetry tells us that $W^s(0)$ is situated above $W^u(0)$ in an exact mirror-image on the other side of the (x_2, p_1)-plane, which is on the right in the bottom part of the picture. The potential intersection looks very different here and so is due to the projection. Indeed, the animation in the multimedia supplement that accompanies this figure shows the manifolds rotating in (x_2, p_1, p_2)-space and there are several frames showing a clear distance between the manifolds in this region [14].

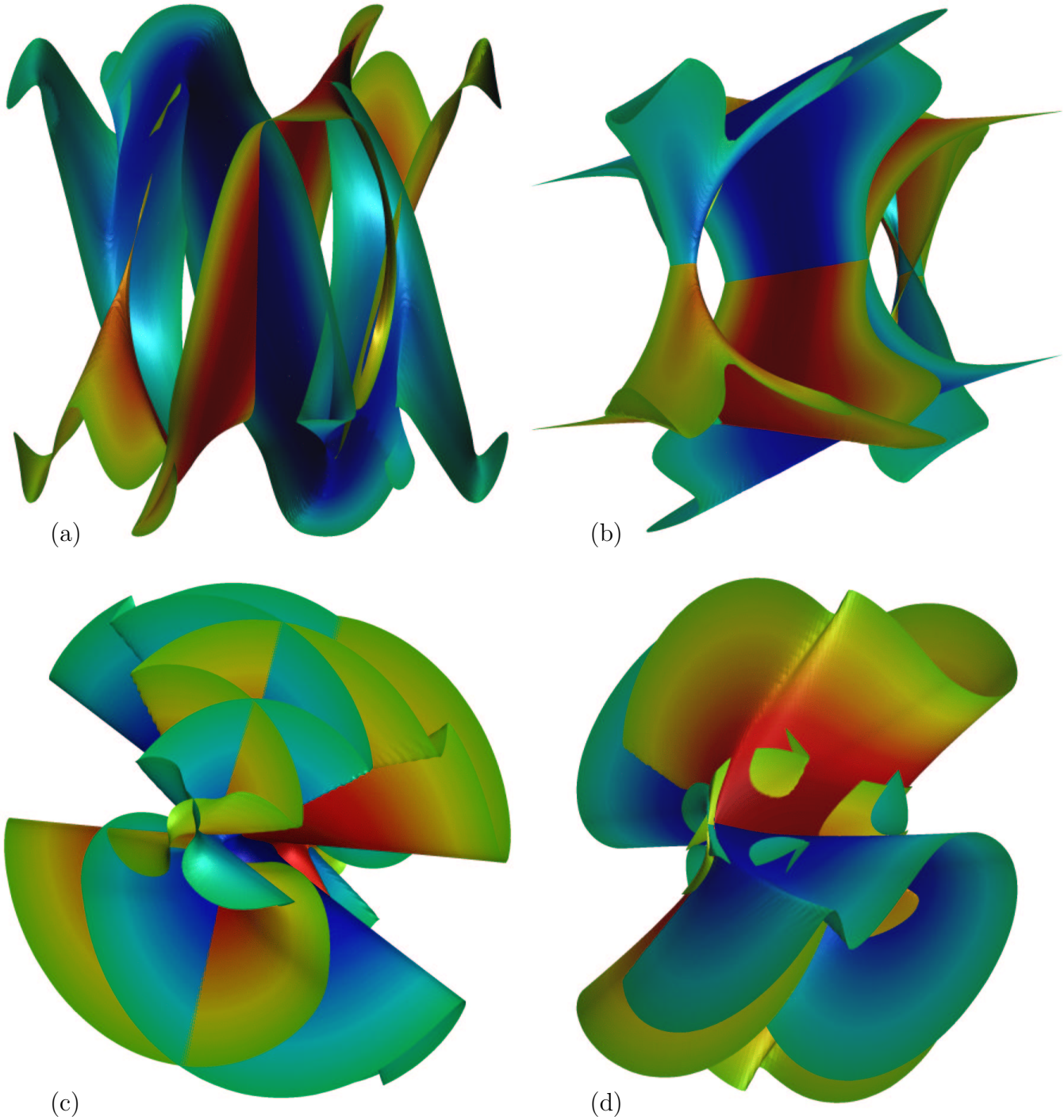

Figure 4: Four different projections of $W^s(0)$ and $W^u(0)$ for Eq. (6) colored according to geodesic distance. The projections are along a coordinate axis onto $p_2 = 0$ (a), $p_1 = 0$ (b), $x_2 = 0$ (c), and $x_1 = 0$ (d), respectively. The same projections were used in Fig. 5, where the manifolds are colored according to the fourth (missing) coordinate.

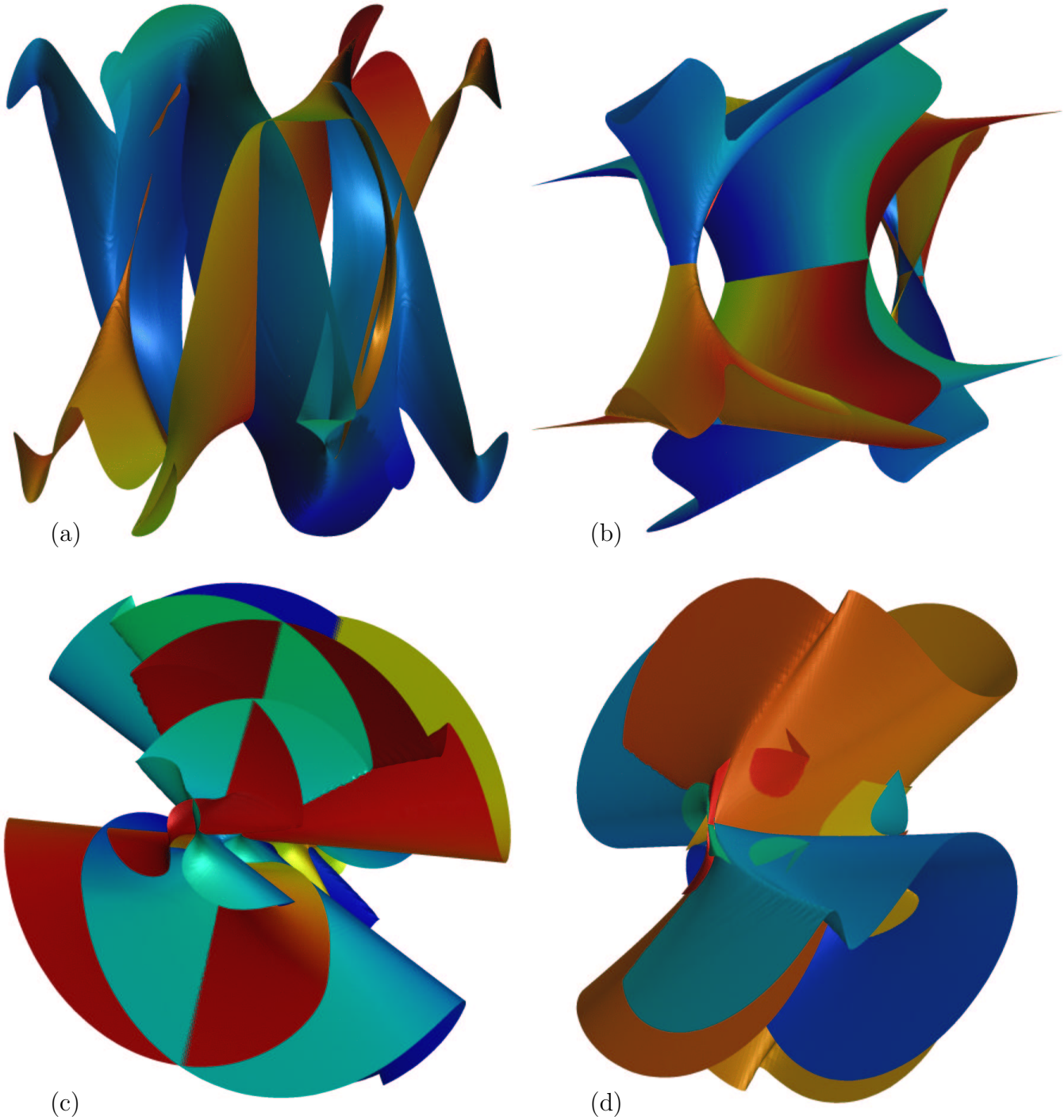

Figure 5: Four different projections of $W^s(0)$ and $W^u(0)$ for Eq. (6) colored according to the fourth (missing) coordinate. The projections are along a coordinate axis onto $p_2 = 0$ (a), $p_1 = 0$ (b), $x_2 = 0$ (c), and $x_1 = 0$ (d), respectively. The same projections were used in Fig. 4, where the manifolds are colored according to geodesic distance.

Note that Figs. 2 and 3 show the same two manifolds. Only the projections are different! Both manifolds are surfaces and it does not seem so hard to try and imagine what these look like in four-dimensional space. However, this turns out to be a lot harder than anticipated. Figure 4 shows four different projections of $W^s(0)$ and $W^u(0)$, each onto a different space, where geodesic distance is used to color the manifolds. In Fig. 4(a) the projection is along the p_2-axis, in panel (b) it is along the p_1-axis, in (c) along the x_2-axis, and in (d) along the x_1-axis. To be more precise, panel (a) shows the same projetion as in Fig. 1. In panel (b) the manifolds are rotated in (x_1, x_2, p_2)-space as follows: a rotation by $-\frac{\pi}{5}$ about the x_2-axis, followed by a rotation of $-\frac{\pi}{30}$ about the x_1-axis and a rotation of $-\frac{\pi}{40}$ about the p_2-axis. The rotations in (x_1, p_1, p_2)-space in panel (c) are $-\frac{9\pi}{20}$ about the x_1-axis, followed by $-\frac{\pi}{12}$ about the p_1-axis and $\frac{7\pi}{25}$ about the p_2-axis. Finally, panel (d) shows the manifolds in (x_2, p_1, p_2)-space with a rotation by $-\frac{3\pi}{5}$ about the x_2-axis and $\frac{5\pi}{24}$ about the p_2-axis.

The same projections are shown in Fig. 5, but now the manifolds are colored using the fourth, missing, coordinate. In Fig. 5(a) colors are as in Fig. 1(b) and (d), with the p_2-coordinate varying between ± 20.0. In Fig. 5(b) the manifolds are colored similarly using the value of the p_1-coordinate, ranging between ± 25.465. The x_2-coordinate is used in panel (c) with a range of ± 11.159 and panel (d) uses the same coloring as in Fig. 3(b), namely a range of ± 10.533 of the x_1-coordinate.

Both Figs. 4 and 5 clearly illustrate the symmetry of the manifolds. In particular, the three seemingly straight lines of intersections between $W^s(0)$ and $W^u(0)$ in Figs. 4(b) and 5(b) lie in the (x_1, p_2)-plane. These same three lines are shown in a different projection in panel (c) of these figures. The intersection with the (x_2, p_1)-plane of symmetry is less pronounced, but can be seen in panels (a) and (d).

5 Conclusions

We discussed the visualization of two-dimensional invariant manifolds in four-dimensional space. While the computation of such manifolds already constitutes a major scientific challenge, the results cannot be interpreted without visualization. In fact, the global stable and unstable manifolds of the origin of the Hamiltonian dynamical system (6) presented here are among the first examples of the computation and visualization of two-dimensional manifolds

in four-dimensional space; the only other example we are aware of is a system of two coupled pendula presented in [2].

The algorithm that we use for the computation of the manifolds has the advantage that the manifolds are grown as a collection of geodesic level sets. Particularly for higher-dimensional systems, the interpretation of the computations is greatly facilitated by using the information on geodesic distance to color the manifolds. This method complements the more common technique of using color for the fourth (missing) coordinate.

The example used in this paper has the added advantage that the stable and unstable manifolds are each other's image under certain symmetry transformations. Hence, by showing both manifolds we, effectively, see the same manifold from two different viewpoints.

We are convinced that visualizations as presented here are an important ingredient for the future use of manifold computations in applications.

Acknowledgments

The author would like to thank Bernd Krauskopf for his helpful suggestions and careful reading of the manuscript.

References

[1] Dellnitz, M. and Hohmann, A., A subdivision algorithm for the computation of unstable manifolds and global attractors. *Num. Math.* **75**, 293–317, 1997.

[2] Guckenheimer, J. and Vladimirsky, A., "A fast method for approximating invariant manifolds" preprint, 2003; available via http://www.math.cornell.edu/∼vlad/papers/InvMfolds/InvMfolds.pdf.

[3] Hauser, J. and Osinga, H. M., *On the geometry of optimal control: the inverted pendulum example*, in Proc. Amer. Control Conf., Arlington VA, June 25-27 (2001), pp. 1721–1726.

[4] Henderson, M. E., "Computing Invariant Manifolds by Integrating Fat Trajectories" IBM Research Report RC22944, 2003.

[5] Jadbabaie, A., Yu, J., and Hauser, J. Unconstrained receding-horizon control of nonlinear systems. *IEEE Trans. Automatic Control*, **46**(5): 776–783, 2001.

[6] Johnson, M. E., Jolly, M. S., and Kevrekidis, I. G. Two-dimensional invariant manifolds and global bifurcations: some approximation and visualization studies. *Numerical Algorithms* **14**: 125–140, 1997.

[7] Krauskopf, B. and Osinga, H. M., Two-dimensional global manifolds of vector fields, *CHAOS*, 1999, **9**(3): 768–774.

[8] Krauskopf, B. and Osinga, H. M., Computing geodesic level sets on global (un)stable manifolds of vector fields, to appear in *SIAM J. Applied Dynamical Systems* **2**(4), 2003.

[9] Kwakernaak, H. and Sivan, R., *Linear optimal control systems*, Wiley-Interscience, New York, 1972.

[10] Palis, J. and De Melo, W., *Geometric Theory of Dynamical Systems*, Springer-Verlag, New York, 1982.

[11] Phillips, M., Levy, S. and Munzner, T., Geomview: An Interactive Geometry Viewer, *Notices of the American Mathematical Society*, 1993, 40:985–988. This software and the accompanying manual are available at `http://www.geom.uiuc.edu/`.

[12] L. S. Pontryagin, V. G. Boltyanski, R. V. Gamkrelidze, and E. F. Mischenko, *The Mathematical Theory of Optimal Processes*, John Wiley & Sons, New York, 1962.

[13] A. J. van der Schaft, *L_2-Gain and Passivity Techniques in Nonlinear Control*, Springer-Verlag, 2nd edition, New York, 2000.

[14] The associated multimedia supplement can be found at `http://www.enm.bris.ac.uk/staff/hinke/cag/`.